High-order harmonic generations in tilted Weyl semimetals

Zi-Yuan Li(李子元)[†], Qi Li(李骐), and Zhou Li(李舟)

GBA Branch of Aerospace Information Research Institute, Chinese Academy of Sciences, Guangzhou 510700, *China*

(Received 23 May 2022; revised manuscript received 1 September 2022; accepted manuscript online 15 September 2022)

We investigate high-order harmonic generations (HHGs) under comparison of Weyl cones in two types. Due to the hyperboloidal electron pocket structure, strong noncentrosymmetrical generations in high orders are observed around a single type-Ⅱ Weyl point, especially at zero frequency. Such a remarkable DC signal is proved to have attributions from the intraband transition after spectral decomposition. Under weak pulse electric field, the linear optical response of a non-tilted Weyl cone is consistent with the Kubo theory. With extensive numerical simulations, we conclude that the non-zero chemical potential can enhance the even-order generations, from the slightly tilted system to the over-tilted systems. In consideration of dynamical symmetries, type-I and type-Ⅱ Weyl cones also show different selective responses under the circularly polarized light. Finally, using a more realistic model containing two pairs of Weyl points, we demonstrate that paired Weyl points with opposite chirality can suppress the overall even-order generations.

Keywords: high order harmonic generation, nonlinear optics, Weyl semimetals

PACS: 42.65.–k, 33.57.+c, 78.20.–e, 78.20.Bh **DOI:** 10.1088/1674-1056/ac9220

1. Introduction

Research of nonlinear optics is mainly accelerated by interactions of intense laser field with materials.[1] As an up-conversion process of photons, high-order harmonic generations (HHGs) represent the extreme nonlinear electron dynamic process interacting with light. The most early non-perturbative HHG was found in the rare gases[2] and the dynamics was explained by the semiclassical three-step model.[3–6] The discovery of nonlinear generations in solid-state materials[7] has attracted a great deal of attention on attosecond pulse generation[8–10] and its potential applications in nano-scale devices.[11–13] HHGs can capture the dynamic information of electrons, which makes it a useful tool to reconstruct the energy band structures[14–17] and to explore topological phase transitions and symmetry breakings.[18–21] The microscopic mechanisms, such as the relationship between cut-off energy and driver laser wavelength, the coupling dynamics of optical inter- and intraband excitation is also being solved.[22–28]

The superior properties of semimetals, such as high carrier mobility, low charge carrier density, low effective mass, and large magnetoresistance bring promising prospect to novel devices.[29,30] As one of the most representative Dirac semimetals (DSMs), graphene shows high conversion efficiencies of terahertz high harmonics,[31–33] which motivates researchers to explore HHGs' control strategy associated with stacked, twisted structures or heterostructures in graphene, graphene-like two-dimensional materials.[34–36] Recently, HHGs in 3D DSM Cd_3As_2 are observed at room temperature,[37] which is considered to be originated from coherent intraband acceleration of Dirac electrons. The quasi-particles in these materials are governed by the Dirac or Dirac-like equations. By breaking either the time-reversal symmetry or inversion symmetry, a single Dirac node can be separated into two Weyl nodes with opposite chirality. Surface Fermi arcs connecting the pair of Weyl points (WPs) have been predicted and observed in both material calculations[38–40] and experiments,[41–46] such as TaAs, TaP, and other Weyl semimetals (WSMs). While the potential energy component in $E(\boldsymbol{k})$ is larger than the kinetic component at some $\boldsymbol{k}$ points, the Weyl cone will be over tilted, with the hyperboloidal electron and hole pockets intersecting at the nodal point. We call it the type-Ⅱ semimetal.[47,48] Owing to the linear energy dispersion and large Berry curvature dipole near the WPs, WSMs are expected to perform strong nonlinear hall responses.[49] Transport measurements on the bilayer, few-layer WTe_2 materials show strong second-order transverse voltage responses under zero magnetic filed. Third-order and even higher-order hall responses are also found in thick Td-$MoTe_2$, $TaIrTe_4$, etc.[50–53] The light-induced anomalous Hall effects are also found in graphene and surfaces of 3D topological insulators.[54–57] The strong photovoltaic process is predicted with the combination of inversion symmetry breaking and tilts of the Weyl cone.[58] Up to now, giant nonlinear optical responses are found in both types of WSMs with broken inversion symmetry, such as the second-harmonic generations in TaAs, WTe_2,[59–61] photocurrent from the circular photogalvanic effect in type-Ⅱ WSMs,[62–64] and high harmonics from WSM WP_2.[65]

Our work focuses on the influence of tilted structures to the high-order harmonics in Weyl semimetal. Numerical evolution of the time-dependent Dirac equation (TDDE) is performed to simulate the electron dynamics with laser.[66–68] In

[†]Corresponding author. E-mail: liziyuan3210087@gmail.com

© 2022 Chinese Physical Society and IOP Publishing Ltd

the type-Ⅱ cones, the electron pocket is occupied, but the hole pocket is unoccupied. The electrons stimulated from such asymmetrical structures exhibit tremendous large direct current (DC) signal, even- and odd-order high harmonic generations. Through the diagonal transformation, we figure out the roles of intraband and interband transitions in the HHGs. Generations in zero and non-zero chemical potential cases are all considered. We also reveal that the selective generations are broken in the over-tilted Weyl cone with a circularly polarized light. In the last part, the nonlinear optical generations are investigated in a lattice model existing two pairs of type-Ⅱ Weyl cones. The sign of chirality determines the superposition effects of harmonics around the cones.

2. hamiltonian and electron dynamics coupling with laser

In a WSM, the conduction and valence bands with linear dispersion touch at Weyl points (WPs). Each WP carries a topological charge of $\pm$, corresponding to its chirality. Consider the most general Hamiltonian describing a Weyl point as follows:[69,70]

$$\hat{H}(\boldsymbol{k}) = \sum_{\substack{i=x,y,z \\ j=x,y,z}} k_i M_{ij} \sigma_j + \boldsymbol{w}\cdot\boldsymbol{k}\mathbb{I}_{2\times 2}, \tag{1}$$

where $\hat{\sigma}_{x,y,z}$ represents the Pauli matrices, $\boldsymbol{k}$ is the wave vectors in three dimensions, M is the matrix of coefficients, and $\boldsymbol{w}$ tilts the dispersion along the $\hat{\boldsymbol{w}}$ direction with $\hat{\boldsymbol{w}} = \boldsymbol{w}/w$. Note that the WPs in WSMs with opposite topological charge are usually not degenerate in energy. Therefore it is possible that only one node near the chemical potential is optically stimulated while another one is Pauli-blocked at sufficiently low energy. To demonstrate the optical responses around the type-I and type-Ⅱ cones, we adopt the continuous model of one Weyl point taken from Ref. [48],

$$\begin{aligned}\hat{H}(\boldsymbol{k}) \;=\; & \gamma(Ak_x + Bk_y) + (ak_x + ck_y)\hat{\sigma}_y \\ & + (bk_x + dk_y)\hat{\sigma}_z + ek_z\hat{\sigma}_x,\end{aligned} \tag{2}$$

where the parameters fitting with the cone band structure are $A = -2.738$, $B = 0.612$, $a = 0.987$, $b = 1.107$, $c = 0.0$, $d = 0.270$, and $e = 0.184$ in units of eV $\cdot$ Å. We multiply γ on the scalar terms to control how tilted the cone is. As γ ranges from 0 to 1, the cone will be tilted from type-I to type-Ⅱ, as shown in Figs. 1(a)–1(c), and it starts to be tangent with the energy surface which passes through the node point, at critical value $\gamma_c \approx 0.173$.

The eigenvalues also contain the tilted and non-tilted parts

$$E_\pm(\boldsymbol{k}) = E_t \pm E_{nt}, \tag{3}$$

specifically

$$E_t = \gamma(Ak_x + Bk_y),$$

$$E_{nt} = \sqrt{e^2k_z^2 + (bk_x + dk_y)^2 + (ak_x + ck_y)^2},$$

and signs $\pm$ refer to the upper and lower bands.

The characteristic difference between the two types of Weyl cones is the pockets' structure as illustrated in Fig. 1(b). For the non-tilted cone ($\gamma = 0$), the edge of the contours stays elliptical and centrosymmetric. While $0 < \gamma < \gamma_c$, it starts to be distorted and uncentrosymmetric but still enclosed. When the tilted parameter is over the critical value γ_c, the electron and hole pockets of the type-Ⅱ cones are formed, in which the boundary of pockets is hyperboloidal and the area of pockets becomes larger with the γ increasing.

To see how the electrons are driven by the laser under such different structures of Weyl cones, we implant the vector potential $\boldsymbol{A}(t)$ of the pulse's electric filed into the electron's momentum terms. Therefore the Hamiltonian in time is given by

$$\hat{H}(\boldsymbol{k}, t) = \hat{H}(\boldsymbol{k} + e_l\boldsymbol{A}(t)), \tag{4}$$

where e_l is the elementary charge. In particular, the vector potential is of the form

$$A_j(t) = \frac{E_0}{\Omega}\exp\left[-2\ln 2\left(\frac{t}{t_0}\right)^2\right]\sin(\Omega t), \tag{5}$$

where j is the polarized direction, E_0 is the peak amplitude of the electric field, Ω is the photon's frequency, and t_0 in the Gaussian envelope function sets to be $5T$ with $T = 2\pi/\Omega$.

The velocity components from both bands are given by $v_x = \gamma A \pm [(a^2 + b^2)k_x + (ac + bd)k_y]/L$, $v_y = \gamma B \pm [(ac + bd)k_x + (c^2 + d^2)k_y]/L$, and $v_z = \pm e^2k_z/L$, with $L = \sqrt{(ak_x + ck_y)^2 + (bk_x + dk_y)^2 + e^2k_z^2}$. Firstly we consider the quasiclassical kinetic approach by replacing the momentum $\boldsymbol{k}$ inside the velocities with $\boldsymbol{k} + e_l\boldsymbol{A}(t)$. Thus, we can describe the electrons' movements by $\boldsymbol{v}(t)$ inside each band. Typically the oscillation happens around the original point o is

$$v_x(t) = \gamma A \pm \mathrm{sgn}(A_x(t))\sqrt{a^2 + b^2}, \tag{6}$$

where the electric field is chosen to be linearly polarized along x direction and the tilted term γA contributes only as constant in the velocities. Considering the unique pocket structure in type-Ⅱ Weyl cone, we also check the upper-band oscillation at point n residing in the electron pocket ($\boldsymbol{k} = [0.002, 0, 0]$ Å^{-1}). Since term γA contributes the same direct signal strength in different $\boldsymbol{k}$, we only discuss the Fourier harmonics of $v_x(t)$'s oscillating part. It is shown in Fig. 1(d) that point o contains all odd Fourier harmonics and the amplitudes fall down slowly. Meanwhile at point n, the electron inside the pocket goes through the Weyl point asymmetrically, therefore both even- and odd-order generations happen.

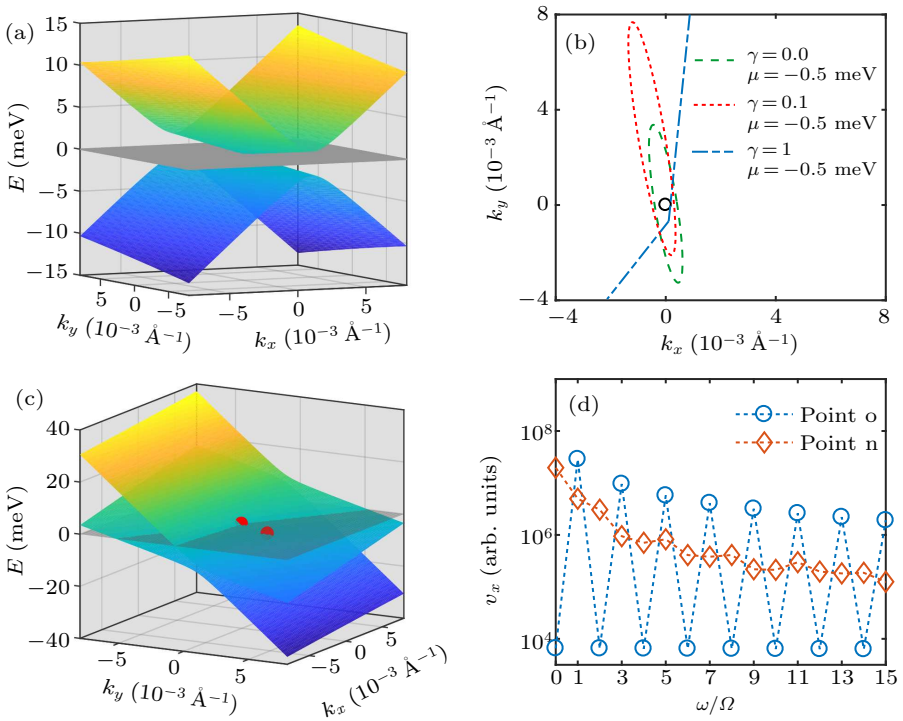


Fig. 1. Schematic of the band structure for (a) non-tilted and (c) over-tilted cones, which refer to the hamiltonian in Eq. (2) with $\gamma = 0$ and $\gamma = 1$, respectively. (b) The valence-band contours at chemical potential $\mu = -0.5$ meV are plotted where the dashed line, dotted line and dot-dashed line correspond to the the cones with different tilt parameters $\gamma = 0$, 0.1, 1, respectively. (d) The Fourier harmonics of $v_x(t)$'s oscillating part at the original point o and one point n on the upper band of the electron pocket, which both marked in (c).

To study the electron dynamics includes both inter- and intraband transitions, we need numerical solutions of the time-dependent Dirac equation for each occupied states in $\boldsymbol{k}$ space[68]

$$\mathrm{i}\hbar\frac{\partial\psi(\boldsymbol{k},t)}{\partial t} = \hat{H}(\boldsymbol{k}+e_l\boldsymbol{A}(t))\psi(\boldsymbol{k},t), \tag{7}$$

which omits the interactions between electrons. Previous works about solving the TDDE focus on the coupling between the intense few-cycle laser and Dirac materials.[71–73] Analytical instantaneous solutions of time-dependent Dirac equation from conduction and valence bands are combined as ansatz substituted into the process of time evolution, from which the temporal variations of the expansion coefficients are further obtained. Here we treat the time evolution process more straightforwardly. The initial electron states from each band are given by the eigenvalues of the $\hat{H}$ without external field and they are evolved independently. We numerically integrate the time-dependent Dirac equation from $-15T$ to $15T$, with applying the 4th-order Runge–Kutta method. The outputs are confirmed almost without changes under smaller discretization. After solving Eq. (7), we can obtain the spinor wave functions $\psi_{c,v}(\boldsymbol{k},t)$ at each time and momentum point, where c and v stand for the conduction and valence bands, respectively.

The electric currents are defined as the expectation values of the operator $\hat{\boldsymbol{j}} = \frac{\partial\hat{H}}{\partial\boldsymbol{A}} = e\hat{\boldsymbol{v}}$, in which group velocity matrices are defined as $\hat{v}_x = \gamma A + a\hat{\sigma}_y + b\hat{\sigma}_z, \hat{v}_y = \gamma B + c\hat{\sigma}_y + d\hat{\sigma}_z$ and $\hat{v}_z = e\hat{\sigma}_x$. In the type-II Weyl cone, the currents can be stimulated both inside the electron pocket (ep) and out of the pockets (op). In the former case, the electron states from both bands are occupied and the currents $\boldsymbol{J}_{\mathrm{ep}}(t)$ can be described as

$$\sum_{\boldsymbol{k}\in\mathrm{ep}} e_l\langle\psi_c(\boldsymbol{k},t)|\hat{\boldsymbol{v}}(\boldsymbol{k})|\psi_c(\boldsymbol{k},t)\rangle + e_l\langle\psi_v(\boldsymbol{k},t)|\hat{\boldsymbol{v}}(\boldsymbol{k})|\psi_v(\boldsymbol{k},t)\rangle.$$

The currents out of pocket are only stimulated from the valence band that is below the chemical potential,

$$\boldsymbol{J}_{\mathrm{op}}(t) = \sum_{\boldsymbol{k}\in\mathrm{op}} e_l\langle\psi_v(\boldsymbol{k},t)|\hat{\boldsymbol{v}}(\boldsymbol{k})|\psi_v(\boldsymbol{k},t)\rangle. \tag{8}$$

The stimulations in the whole area are $\boldsymbol{J}(t) = \boldsymbol{J}_{\mathrm{ep}}(t) + \boldsymbol{J}_{\mathrm{op}}(t)$.

3. Numerical comparison in two types of Weyl cones

3.1. HHG responses with zero chemical potential

With chemical potential through the nodal energy ($E = 0$), the non-tilted ($\gamma = 0$) and over-tilted ($\gamma = 1$) Weyl cones are mostly differentiated by the hyperboloidal electron and hole pocket structure. Electron states from the electron pocket are stimulated from both bands but in noncentrosymmetrical $\boldsymbol{k}$ positions, thus the generated $J_{\mathrm{ep}}(t)$ are expected to have asymmetrical responses.

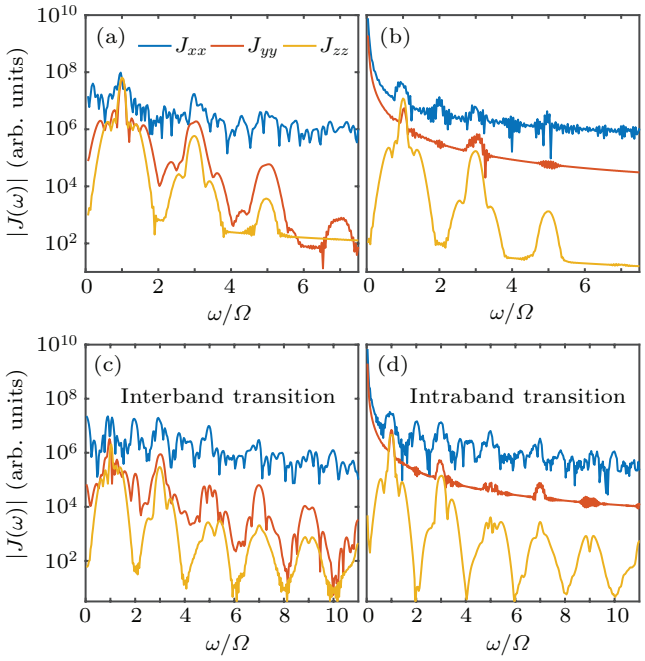


Fig. 2. High harmonic generations of the longitudinal currents by inputting the electric field in three dimensions. (a) and (b) The spectra from the non-tilted and over-tilted Weyl cones. The strength of electric field in the simulation is $E_0 = 2.4$ kV/cm and photon energy $\hbar\Omega$ is 3 meV with $\Omega = 0.72$ THz. J_{xx}, J_{yy}, and J_{zz} are plotted in blue, red, and yellow colors. (c) and (d) Decomposed from the HHGs of the over-tilted cones in (b), illustrating the intraband and interband transitions, respectively.

Coupling with the linearly polarized pulse in each dimension, we observe the anisotropic longitudinal HHG responses as shown in Fig. 2. In the non-tilted cone (a), the stimulated current J_{xx} holds broader spectral width than other directions due to its larger Fermi velocity. Each direction's inversion symmetry is kept in the this case, therefore we only observe the odd-order generations. In the over-tilted case, since the states inside the electron pocket distribute without centrosymmetry along x and y directions, we observe both odd- and even-order generations in these two directions. The currents perform odd-only generations in z direction where the centrosymmetry through the Weyl point is always preserved. Significant large currents at frequency zero are generated in x and y directions, which originates from the nonlinear difference frequency process of the even-order harmonic generations. To understand this large direct current, it is efficient to separate the HHGs as intraband and interband transitions. Here, we use the unitary transformation $\mathcal{U}(t)$ to diagonalize the instantaneous hamiltonian $\hat{H}(\boldsymbol{k},t)$. We name the terms in Eq. (2) as

$$\begin{aligned} C_0 &= \gamma(Ak_x + Bk_y), \quad C_1 = ek_z, \\ C_2 &= ak_x + ck_y, \qquad C_3 = bk_x + dk_y, \end{aligned} \tag{9}$$

and $L = \sqrt{C_1^2 + C_2^2 + C_3^2}$ for simplified purpose. Replace k_i with $k_i + e_l A_i(t)$ and the unitary matrix $\mathcal{U}(t)$ explicitly reads

$$\mathcal{U}(t) = \begin{pmatrix} \frac{C_1(t) - iC_2(t)}{\sqrt{2(L(t)+C_3(t))L(t)}} & \frac{C_1(t) - iC_2(t)}{\sqrt{2(L(t)-C_3(t))L(t)}} \\ -\frac{\sqrt{L(t)+C_3(t)}}{\sqrt{2L(t)}} & \frac{\sqrt{L(t)-C_3(t)}}{\sqrt{2L(t)}} \end{pmatrix}. \tag{10}$$

The current operators after the same transformation are given by $\tilde{\hat{j}}_i = \mathcal{U}(t)^{-1}\hat{j}_i\mathcal{U}(t)$, in which we denote the diagonal elements to contribute to the intraband transitions and the off-diagonal elements for the interband transitions. Thus, the intraband and interband transitions could be decoupled. Figures 2(d) and 2(e) illustrate the interband and intraband transitions in the over-tilted cone, respectively. Intuitively, the intraband transition has significant contributions to the direct currents in the over-tilted case. This conclusion echoes the Fourier harmonics of $v_x(t)$ at point n, which is shown in Fig. 1(d). The breaking of inversion symmetry is reflected at both transition processes, i.e., x- and y-direction currents show generations in all orders meanwhile the z-direction currents keep only odd generations.

It is interesting to check whether the linear response of the calculated electron currents fits the kubo formula's predication, especially under weak electric field. This comparison is performed in a non-tilted Weyl cone by setting velocity parameters of hamiltonian in Eq. (2) as $\gamma = 0$ and $a = 1$, $b = 0$, $c = 0$, $d = 1$, and $e = 1$ in units of eV·Å. We apply the Kubo formula as the the correlation function of velocities and spectra functions to express the longitudinal optical conductivity in x direction,

$$\begin{aligned} \sigma_{xx}(\Omega) = \frac{e_l^2}{\Omega\pi}\int_{-\infty}^{+\infty} \mathrm{d}\omega'[f(\omega') - f(\omega'+\Omega)] \\ \times \int \frac{\mathrm{d}\boldsymbol{k}}{(2\pi)^3}\mathrm{Tr}[\hat{v}_x\hat{A}(\boldsymbol{k},\omega')\hat{v}_x\hat{A}(\boldsymbol{k},\omega'+\Omega)], \end{aligned} \tag{11}$$

where $f(\omega')$ is the Fermi–Dirac function with chemical potential μ and temperature at 0.1 K, $\hat{v}_x$ is the x-direction velocity operator and spectra function $\hat{A}(\boldsymbol{k},\omega')$ is obtained from the matrix Green function by the same derivation process in Ref. [74]. Finally we can obtain the interband longitudinal conductivity σ_{xx} and its real part, as plotted in Fig. 3, under different chemical potentials. To have a better matching with the linear response theory, we choose a weak-field pulse 240 V/cm to simulate the currents in the x direction. In the numerical calculations of HHGs, we define the amplitude strength $A_n(\Omega) = \int_{(n-1/2)\Omega}^{(n+1/2)\Omega} \frac{\mathrm{d}\omega}{\Omega} J(\omega)$ for the n-th generation, where the linear response strength of current takes the shadow area in the insert figure. By varying the photon energy during the stimulation, we notice that two distinct slope variations of A_1 occur exactly on $\hbar\Omega = 2$ and 4 meV positions, which are twice the chemical potentials $|\mu|$, respectively. Comparing the numerical results with the theoretical curves, we can find that they share the similar tendency especially when the photon energy

is beyond $|2\mu|$. Such a way of comparing may further expand to the exploration on the nonlinear optical responses.

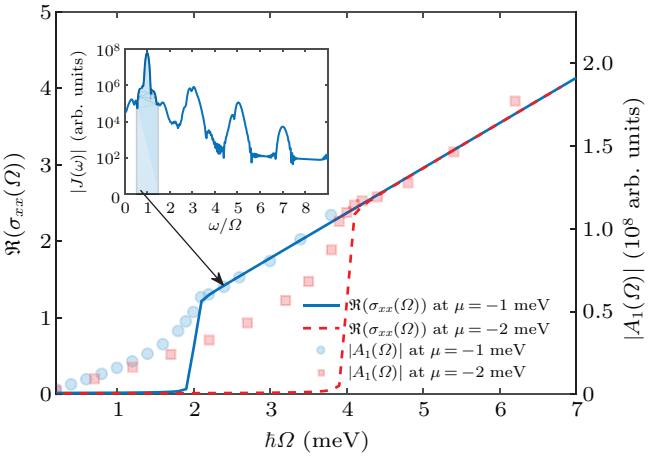


Fig. 3. A comparison between the linear response's strength $A_1(\Omega)$ and the Kubo formula's results, in a non-tilted Weyl cone. The blue solid line and red dashed line represent the real parts of the longitudinal optical conductivity σ_{xx} at $\mu=-1$, -2 meV. Blue circles and red squares correspond to the linear response's strength $A_1(\Omega)$ at $\mu=-1$, -2 meV and under different photon energy $\hbar\Omega$, in which the insert figure shows the example with $\hbar\Omega=2.4$ meV ($\Omega=0.58$ THz) and the shadow area refers to the linear response $A_1(\Omega)$. Note we take the relatively weak electric field 240 V/cm to simulate the optical responses.

3.2. HHG responses with non-zero chemical potential

In the last subsection, we conclude that the unusual HHG responses can reflect the asymmetric stimulations due to the hyperboloidal pocket structure in type-Ⅱ cone with chemical potential at nodal energy. To elucidate how the non-zero chemical potential influences high order generations, we evolve the electron dynamics below the nodal energy. In this discussion, we show that noncentrosymmetric generations can be enhanced in both tilted type-I and type-Ⅱ cones.

Consider a slightly tilted cone $\gamma=0.01$, and the stimulations are driven by the pulse with photon energy 2 meV and electric field strength 1.2 kV/cm. Figure 4(a) shows that the even-order generations are barely seen with zero chemical potential, which is gradually enhanced by the chemical potential changing from 0 to -2 meV. Especially, the generations in even orders are strongly stimulated while $2|\mu|$ equals one photon and two photons' energy. With decreasing the chemical potential continuously, we find that the zero and second-order generations at $\mu=-1$ and -2 meV reach their highest performance, which presents evident Fermi resonances peaks of one photon and two photon process in Fig. 4(b). When fixing the chemical potential at -1.5 meV, the pick-out cases in Fig. 4(c) show that, with tiny tilt ($\gamma=0.01$), a remarkable enhancement of even-order generations happens. Further increasing the tilt either in type-I ($\gamma=0.11$) or type-Ⅱ ($\gamma=1$), the responses approach saturation quickly. In Fig. 4(d), we observe the responses at zero, second and fourth orders rise fast following the tilt increasing, even before the band structure is over tilted (before γ_c). Note the odd-order generations are not changed much with the tilt increasing.

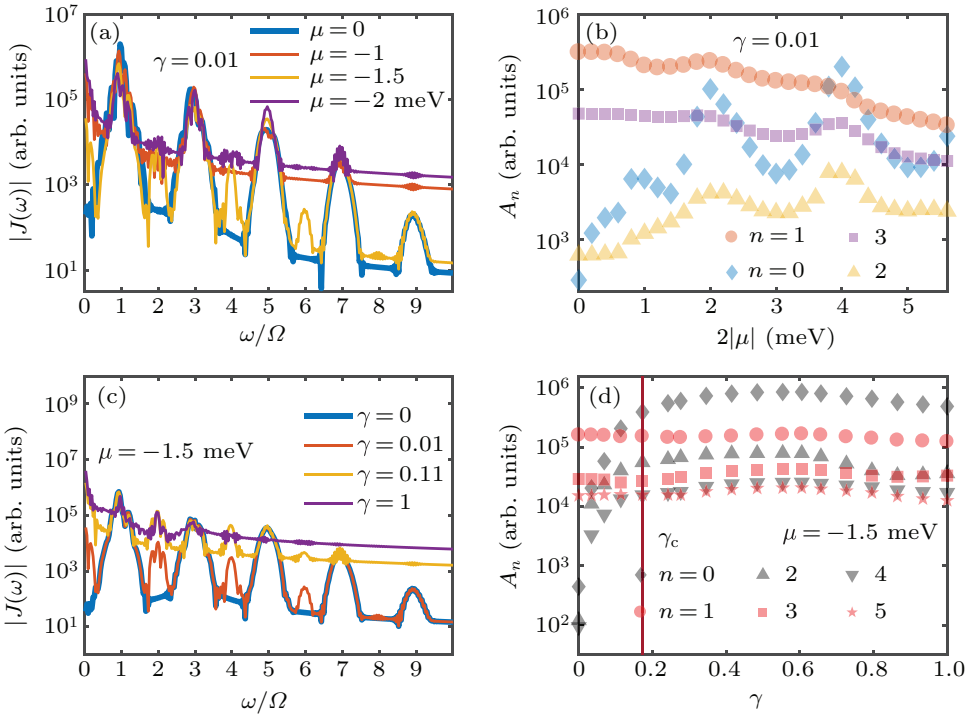


Fig. 4. Subplots (a) and (b), the HHGs in a slightly tilted cone ($\gamma=0.01$) with different chemical potentials. In (a), the curves with blue, red, yellow and purple colors refer to the chemical potentials at $\mu=0$, -1, -1.5, and -2 meV. (b) Showing how the amplitude in each order trends with the continuous change of $|2\mu|$. (c) and (d) The HHGs ranging from type-I to type-Ⅱ cones, by the pulses with photon energy $\hbar\Omega=2$ meV ($\Omega=0.48$ THz) and chemical potential fixed at -1.5 meV. (c) The curves of Weyl cones with $\gamma=0$, 0.01, 0.11, 1 (blue, red, yellow and purple lines). (d) The amplitude strength from each order plotted with the changing of tilt. The solid line marks the critical value γ_c divided by type-I and type-Ⅱ cones.

3.3. Selective generations broken in the type-II cone

In the limit $t_0 \to \infty$, we can treat our discussing object as a time-periodic Floquet system, in which the dynamical symmetry is crucial.[75] As the non-perturbative Floquet process, HHGs can directly reflect the dynamical symmetry of the system. We introduce the vector potential of a left-handed circularly polarized light into the system

$$\boldsymbol{A}(t) = \frac{E_0}{\Omega}\exp\left[-2\ln 2\left(\frac{t}{t_0}\right)^2\right][(\boldsymbol{e}_x\cos(\Omega t)+\boldsymbol{e}_y\sin(\Omega t)]. \tag{12}$$

By implanting the electric filed in x–y plane, the HHG currents at three directions are plotted in Fig. 5. For the non-tilted system (a), the odd-only generations happen in the x, y directions and even-only generations happen in the z direction. Such phenomena of selective generations are related to the Hamiltonian symmetry C_{2z}, which rotates π about the z axis. This symmetry is only preserved in hamiltonian when $\gamma = 0$ in Eq. (2). The dynamical symmetry of the time-dependent hamiltonian needs to consider both the C_{2z} symmetry and the property of vector potential in time translations $\boldsymbol{A}(t) = -\boldsymbol{A}(t+\frac{T}{2})$ at the continuous wave approximation ($t_0 \to \infty$). The details of symmetry analysis to the hamiltonian, currents, states and the selection rules' provement are shown in Appendix A.

For the over-tilted case, the hyperboloid pocket structure breaks the C_{2z} symmetry in hamiltonian and the currents can not be composed as pairwise Floquet states with opposed momentum. With selection rules broken, we can see that the even- and odd-only responses in HHGs are not held anymore, as plotted in Fig. 5(b).

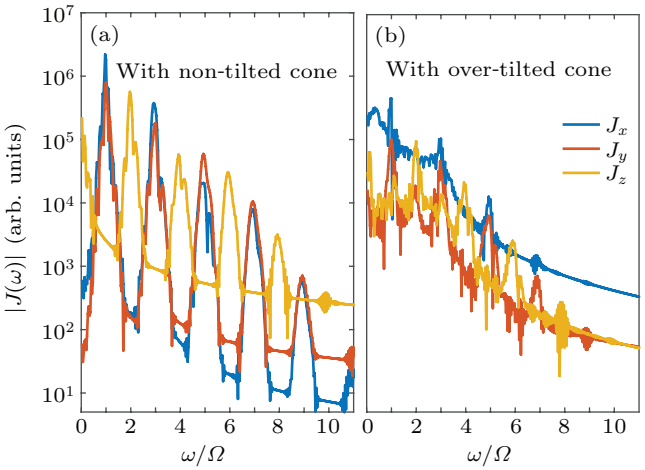


Fig. 5. Currents induced by the left-handed circularly polarized light in the x–y plane, with photon energy $\hbar\Omega = 2$ meV ($\Omega = 0.48$ THz) and electric field strength 1.2 kV/cm. In the non-tilted cone (a), the odd-only generations happen in the x, y directions (blue and red lines) and even-only generations happen in the z direction (yellow line). In the over-tilted cone (b), HHGs of the three directions are stimulated in every order.

Dynamical symmetry has similar impact on the selective generations of transverse currents with linearly polarized light. In Fig. A1(a) for the non-tilted case, the x-direction transverse current J_{xy} induced by the y-direction pulse shows odd-only generations and the z-direction transverse current J_{zy} shows even-only generations. We notice an interesting correspondence between the transverse currents and the currents induced by the circularly polarized light. Explicitly, J_{xy} has the same selection rules with J_x, J_y in Fig. 5(a) while J_{zy} is consistent with the J_z current. Such interesting correspondence can be explained by the same dynamical analysis in Appendix A. As for the over-tilted case, C_{2z} symmetry is no longer held and selective rules are broken as well.

3.4. HHGs from the pairs of Weyl points

In the lattice system, the 'no-go theorem' requires that the Weyl fermions appear in pairs with opposite chirality. Therefore it is necessarily further considered that the nonlinear responses include multiple Weyl points. Here we discuss a lattice model with two pairs of node

$$\begin{aligned}\hat{H}(\boldsymbol{k}) \;=\; & \gamma[\cos(2ak_x)-\cos(ak_0)][\cos(ak_y)-\cos(ak_0)]\hat{\sigma}_0\\ & -\{m[1-\cos^2(ak_y)-\cos(ak_z)]\\ & +2t_x[\cos(ak_x)-\cos(ak_0)]\}\hat{\sigma}_x\\ & -2t\sin(ak_z)\hat{\sigma}_y-2t\cos(ak_y)\hat{\sigma}_z,\end{aligned} \tag{13}$$

in which four nodes located at $(\pm\pi/2a, \pm\pi/2a, 0)$ break inversion symmetry.[76] In Fig. 6(a), the over-tilted structure's parameters are chosen as $t_x = \frac{t}{2}$, $m = 2t$, and $\gamma = 2.7t$, with $t = 40$ meV, $a = 75$ Å. The pocket structures at the nodal energy are plotted in blue (electron) and pink (hole) colors in Fig. 6(b). Note that the Weyl points A and B have the same chirality, while the points C and D are their counterparts with opposed chirality.

To drive the pocket electrons across the Weyl points, we applied the linearly polarized laser in y direction. Figure 6(c) shows the local nonlinear responses around one Weyl point and their superposition effects are associated with the chirality. For a single Weyl point A, the nonlinear harmonics are strong in each order, especially the large direct current, which agrees with the major features on the former type-II cone analysis. Through the current amplitude ratio illustration in (c), we have a quantified understanding over the superposition effects. While we combine the currents around two points with same chirality (A and B), the amplitude strength on each order is doubled. However, for the mixture of two points with opposed chirality (A and C), the odd-order amplitude strength is still enhanced twice, meanwhile the even-order generations are totally weakened. For example, the strength at second harmonic is two orders of magnitude weaker than the single point A, similar to the signal at zero frequency. Due to the cancelation effects between opposed chirality, we cannot observe strong noncentrosymmetric even-order harmonics in this

type-Ⅱ model as verified by the HHGs containing four points in Fig. 6(c). In comparison of the whole Brillouin zone current responses, we should note that the odd-order generations including only the Weyl points' pockets contributions show similar structures with weaker magnitude. In the perspective of numerical calculations with discretization $100\times100\times100$, there are 1014766 states stimulated in the whole Brillouin zone, from which the 6632 states are inside the electron pockets of Weyl points. Therefore, the pockets' area proportion to the whole Brillouin zone has significant impact on the optical nonlinear generations. For the non-tilted circumstance ($\gamma=0$), the Fermi surface is mainly nonsymmetric along the x direction. With pulse on this direction, we observe the stimulated even-order high harmonic generations shown in Fig. B1 in Appendix B.

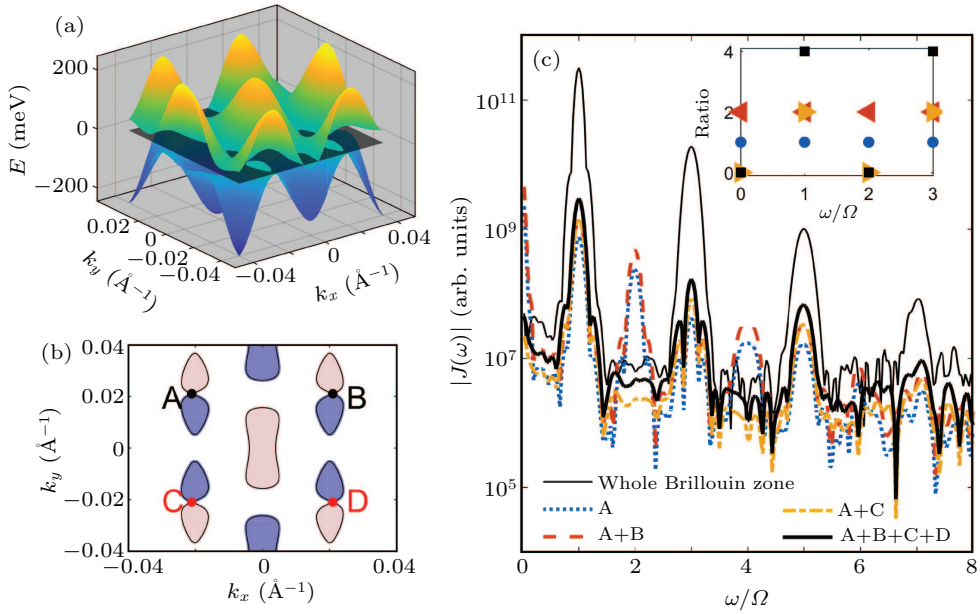


Fig. 6. (a) The band structure of a type-Ⅱ Weyl semimetal at the $k_z=0$ plane, which includes two pairs of Weyl points. (b) The the location of electron (in blue) and hole pockets (in pink), where A and B share the same chirality that C and D have the opposed chirality. (c) The y-direction currents with $\hbar\Omega=3$ meV that $\Omega=0.72$ THz. In particular, dotted line shows the contribution around the electron pocket of one single Weyl point A. Dashed and dot-dashed lines show the results of two Weyl points with same chirality and with opposed chirality. The thick black line is for the total contribution of the electrons pockets around the Weyl points. The thinner black line represents the HHGs from the whole Brillouin zone. The inset in (c) shows the ratio of amplitude strength A_n in different summations to A_n containing only one single Weyl cone A (marked in circle), in which $n=0$, 1, 2, 3 refer to the harmonic orders, left triangles, right triangles, squares refer to the summations A + B, A + C, and A + B + C + D with the same color indices of the lines.

4. Conclusion

The main accomplishments of this paper are as follows. The high harmonic generations from WSMs are investigated both in the continuous model of a single Weyl cone and the lattice model with Weyl points in pairs. By modeling carrier dynamics inside the hyperboloid pocket structure of type-Ⅱ cone, we observe strong noncentrosymmetric HHGs along with the large DC signal. By separating the HHGs into interband and intraband transitions, we conclude that the direct currents are contributed mostly by the latter part. Meanwhile even-order generations are observed in both transitions due to the inversion symmetry broken. In spite of tilting the cone, varying chemical potential below nodal energy could also efficiently enhance the even-order generations, which can be intuitively seen even in a slightly tilted cone. Also, strong Fermi resonances at zero- and second-order harmonics happen while $|2\mu|$ changes to one- or two-photon energy.

Selective generations are investigated through introducing the left-handed circularly polarized light. The selective rule is valid in the non-tilted case since Hamiltonian's dynamical symmetry is kept. In contrast, the over-tilted structure destroys the C_{2z} symmetry which induces all-order generations without selections.

From a more realistic point of view, we consider a lattice model that holds two pairs of Weyl points. The numerical simulations conclude that Weyl points with same chirality double the response strength, while the Weyl points with opposed chirality show enhancement in odd harmonics and cancellation in even harmonics, i.e., the non-centrosymmetric nonlinear responses are suppressed. In the whole Brillouin zone, odd-order generations dominate the optical nonlinear responses. Recent experiments on the tilted Weyl semimetals share similar nonlinear optical signatures with our results. Large shift currents are observed in the type-Ⅱ Weyl semimetal $TaIrTe_4$,[64] which are understood as a third-order nonlinear process combining the in-plane dc field arising from space charge and the optical excitation. The direct optical responses are also found in the tilted semimetal TaAs[77,78] by linearly and circularly polarized lights. They are theo-

retically explained by the photogalvanic effects, the second-order difference-frequency processes. High-harmonic generations of type-Ⅱ Weyl semimetal are reported in β-WP_2 crystals, in which both odd- and even-generations are considered as intraband transitions.[65] The even-order generations are attributed to the spike berry curvature around the Weyl points with broken inversion symmetry. Our results provide a deeper understanding of nonlinear optical responses based on the remarkable features of tilted semimetals and we will promote the study to other novel structures such as nodal line semimetal and hybrid semimetal.

Appendix A: Dynamical symmetry and selection rules

The non-tilted cone's hamiltonian ($\gamma = 0$) in Eq. (2) preserves symmetry C_{2z}, i.e.,

$$h(\boldsymbol{k}) = C_{2z}h(\boldsymbol{k}')C_{2z}^{\dagger}, \tag{A1}$$

where $\boldsymbol{k}' = (-k_x, -k_y, k_z)$. In the following discussions, we use the approximation $t_0 \to \infty$ that $\boldsymbol{A}(t)$ holds continuous wave's form and have the time translation property $\boldsymbol{A}(t) = -\boldsymbol{A}(t + \frac{T}{2})$.

Consider a circularly polarized light in x–y plane is implanted into the system and the time-dependent hamiltonian $h(\boldsymbol{k},t)$ preserves such a dynamical symmetry,

$$h(\boldsymbol{k},t) = C_{2z}h(\boldsymbol{k}',t+T/2)C_{2z}^{\dagger}. \tag{A2}$$

The currents under such operation satisfy

$$\begin{aligned} j_x(\boldsymbol{k},t) &= -C_{2z}j_x(\boldsymbol{k}',t+T/2)C_{2z}^{\dagger}, \\ j_y(\boldsymbol{k},t) &= -C_{2z}j_y(\boldsymbol{k}',t+T/2)C_{2z}^{\dagger}, \\ j_z(\boldsymbol{k},t) &= C_{2z}j_z(\boldsymbol{k}',t+T/2)C_{2z}^{\dagger}. \end{aligned} \tag{A3}$$

The time-dependent quantum equation (TDQE) is

$$\mathrm{i}\hbar\frac{\partial\psi(\boldsymbol{k},t)}{\partial t} = h(\boldsymbol{k},t)\psi(\boldsymbol{k},t). \tag{A4}$$

Substitute the dynamical symmetry relations Eq. (A2) into Eq. (A4) and make the time translation $t \to t - \frac{T}{2}$, then it changes to

$$\mathrm{i}\hbar\frac{\partial C_{2z}^{\dagger}\psi(\boldsymbol{k},t-\frac{T}{2})}{\partial t} = h(\boldsymbol{k}',t)C_{2z}^{\dagger}\psi\left(\boldsymbol{k},t-\frac{T}{2}\right). \tag{A5}$$

The TDQE at $\boldsymbol{k}'$ point is written as

$$\mathrm{i}\hbar\frac{\partial\psi(\boldsymbol{k}',t)}{\partial t} = h(\boldsymbol{k}',t)\psi(\boldsymbol{k}',t). \tag{A6}$$

Comparing Eq. (A5) with Eq. (A6) and suppose that there is no degeneracy, then the eigenfunctions are connected as

$$\psi(\boldsymbol{k}',t) = C_{2z}^{\dagger}\psi\left(\boldsymbol{k},t-\frac{T}{2}\right). \tag{A7}$$

Owing to the periodicity in time, the general solution of TDQE in Floquet theorem is

$$\psi_m^{\mathrm{F}}(\boldsymbol{k},t) = \mathrm{e}^{-\mathrm{i}E_m^{\mathrm{F}}(\boldsymbol{k})t}\boldsymbol{u}_m(\boldsymbol{k},t), \tag{A8}$$

where $E_m^{\mathrm{F}}(\boldsymbol{k})$ represents the Floquet eigenvalues that satisfy $E_m^{\mathrm{F}}(\boldsymbol{k}) = E_m^{\mathrm{F}}(\boldsymbol{k}')$ in the non-tilted case, $\boldsymbol{u}_m(\boldsymbol{k},t)$ is a T-periodical function, and m is the band index. Through the derivations of Eqs. (A4)–(A6), we obtain the relations of Floquet states just like Eq. (7) as follows:

$$\psi_m^{\mathrm{F}}(\boldsymbol{k}',t) = C_{2z}^{\dagger}\psi_m^{\mathrm{F}}\left(\boldsymbol{k},t-\frac{T}{2}\right). \tag{A9}$$

We project the electric currents j_α into the m-th pairwise Floquet states

$$\begin{aligned} J_m^{\alpha}(\boldsymbol{k},t) = {}& \psi_m^{F\dagger}(\boldsymbol{k},t)j_\alpha(\boldsymbol{k},t)\psi_m^{\mathrm{F}}(\boldsymbol{k},t) \\ & + \psi_m^{F\dagger}(\boldsymbol{k}',t)j_\alpha(\boldsymbol{k}',t)\psi_m^{\mathrm{F}}(\boldsymbol{k}',t). \end{aligned} \tag{A10}$$

Substituting Eqs. (A3) and (A9) into Eq. (A10), we can find the connection as follows:

$$\begin{aligned} J_m^x(\boldsymbol{k},t) &= -J_m^x(\boldsymbol{k},t+T/2), \\ J_m^y(\boldsymbol{k},t) &= -J_m^y(\boldsymbol{k},t+T/2), \\ J_m^z(\boldsymbol{k},t) &= J_m^z(\boldsymbol{k},t+T/2). \end{aligned} \tag{A11}$$

The n-th order harmonic generation in x direction with considering the symmetry of currents in Eq. (A11) is

$$\begin{aligned} J_m^x(\boldsymbol{k},n\Omega) &= \int_0^T \frac{\mathrm{d}t}{T}\mathrm{e}^{\mathrm{i}n\Omega t}J_m^x(\boldsymbol{k},t) \\ &= \int_0^T \frac{\mathrm{d}t}{T}\mathrm{e}^{\mathrm{i}n\Omega(t+\frac{T}{2})}J_m^x\left(\boldsymbol{k},t+\frac{T}{2}\right) \\ &= -\mathrm{e}^{\mathrm{i}n\pi}J_m^x(\boldsymbol{k},n\Omega). \end{aligned} \tag{A12}$$

Similarly we obtain $J_m^y(\boldsymbol{k},n\Omega) = -\mathrm{e}^{\mathrm{i}n\pi}J_m^y(\boldsymbol{k},n\Omega)$ and $J_m^z(\boldsymbol{k},n\Omega) = \mathrm{e}^{\mathrm{i}n\pi}J_m^z(\boldsymbol{k},n\Omega)$. The selection rules are obvious: $J_m^{x,y}(\boldsymbol{k},n\Omega) = 0$ when n is even number; $J_m^z(\boldsymbol{k},n\Omega) = 0$ when n is odd number. Sum the currents in each band, then we will have the same selective generations.

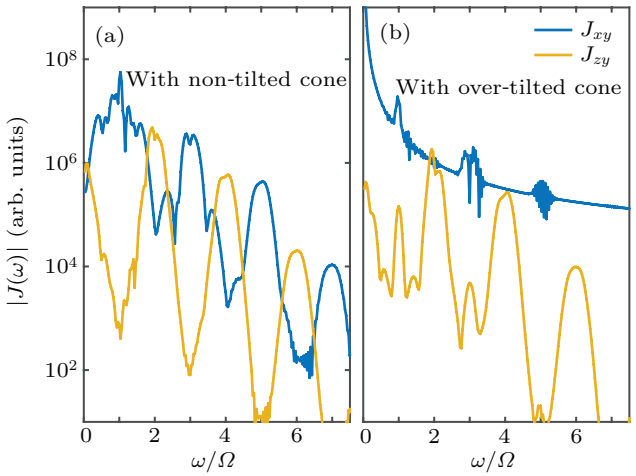


Fig. A1. Transverse currents stimulated by the y-direction polarized pulse in the non-tilted ($\gamma = 0$) and over-tilted ($\gamma = 1$) cones. In (a), the transverse current J_{xy} in x direction shows odd-only generations (blue line) and current J_{zy} in z direction shows even-only generations (yellow line). The correspondent cases in the over-tilted cone ($\gamma = 1$) are shown in (b).

In the type-Ⅱ cones, the symmetry C_{2z} is not held anymore and we see the HHGs happen in each order. The former dynamical analysis about circularly polarized light can also be applied into the linearly polarized case. In the non-tilted case, the transverse currents stimulated by the y-direction polarized light also show selective generations that odd orders in the x direction and even orders in the z direction (Fig. A1). In the over-tilted generations, we can see from Fig. A1(b) that selective generations are destroyed without holding the dynamical symmetry.

Appendix B: Nonlinear optical responses in a non-tilted lattice model

Figure B1 shows the nonlinear optical responses in the non-tilted lattice model (with $\gamma = 0$ in Eq. (13)). The Fermi surface around each Weyl point is distorted and asymmetric along the x direction. The longitudinal HHGs illustrate the even-order responses in this direction besides the intense odd-order generations.

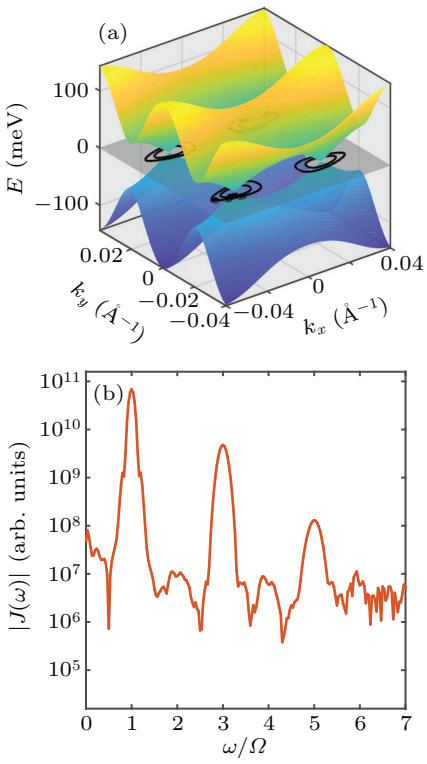


Fig. B1. (a) The band structure of the non-tilted type-I Weyl semimetal at $k_z = 0$ plane, described in Eq. (13). The contour lines show the distorted Fermi surfaces around the Weyl points that are asymmetric along x direction. (b) The HHGs are stimulated by the x-polarized pulse with energy $\hbar\Omega = 3$ meV. Odd- and even-order generations are all stimulated, with the broken inversion symmetry.

Acknowledgements

We thank Tatsuhiko N. Ikeda for illuminating discussions. This work was performed at the Chinese Academy of Science Terahertz Science Center, and was supported by the National Natural Science Foundation of China (Grant No. 61988102).

References

[1] Boyd R W 2020 *Nonlinear Optics* (New York: Academic Press)
[2] McPherson A, Gibson G, Jara H, Johann U, Luk T S, McIntyre I, Boyer K and Rhodes C K 1987 *J. Opt. Soc. Am. B* **4** 595
[3] Krause J L, Schafer K J and Kulander K C 1992 *Phys. Rev. Lett.* **68** 3535
[4] Schafer K, Yang B, DiMauro L and Kulander K 1993 *Phys. Rev. Lett.* **70** 1599
[5] Corkum P B 1993 *Phys. Rev. Lett.* **71** 1994
[6] Ghimire S and Reis D A 2019 *Nat. Phys.* **15** 10
[7] Ghimire S, DiChiara A D, Sistrunk E, Agostini P, Di-Mauro L F and Reis D A 2011 *Nat. Phys.* **7** 138
[8] Vampa G and Brabec T 2017 *J. Phys. B: At. Mol. Opt. Phys.* **50** 083001
[9] Garg M, Kim H Y and Goulielmakis E 2018 *Nat. Photon.* **12** 291
[10] Li J, Lu J, Chew A, Han S, Li J, Wu Y, Wang H, Ghimire S and Chang Z 2020 *Nat. Commun.* **11** 2748
[11] Sivis M, Duwe M, Abel B and Ropers C 2013 *Nat. Phys.* **9** 304
[12] Han S, Kim H, Kim Y W, Kim Y J, Kim S, Park I Y and Kim S W 2016 *Nat. Commun.* **7** 13105
[13] Vampa G, Ghamsari B, Siadat Mousavi S, *et al.* 2017 *Nat. Phys.* **13** 659
[14] Vampa G, Hammond T, Thiré N, Schmidt B, Légaré F, McDonald C, Brabec T, Klug D and Corkum P 2015 *Phys. Rev. Lett.* **115** 193603
[15] Tancogne-Dejean N, Mücke O D, Kärtner F X and Rubio A 2017 *Phys. Rev. Lett.* **118** 087403
[16] Lanin A, Stepanov E, Fedotov A and Zheltikov A 2017 *Optica* **4** 516
[17] Li L, Lan P, He L, Cao W, Zhang Q and Lu P 2020 *Phys. Rev. Lett.* **124** 157403
[18] Silva R, Jiménez-Galán Á, Amorim B, Smirnova O and Ivanov M 2019 *Nat. Photon.* **13** 849
[19] Chacón A, Kim D, Zhu W, *et al.* 2020 *Phys. Rev. B* **102** 134115
[20] Schmid C P, Weigl L, Grössing P, *et al.* 2021 *Nature* **593** 385
[21] Bai Y, Fei F, Wang S, Li N, Li X, Song F, Li R, Xu Z and Liu P 2021 *Nat. Phys.* **17** 311
[22] Golde D, Meier T and Koch S W 2008 *Phys. Rev. B* **77** 075330
[23] Vampa G, McDonald C, Orlando G, Klug D, Corkum P and Brabec T 2014 *Phys. Rev. Lett.* **113** 073901
[24] Vampa G, McDonald C, Orlando G, Corkum P and Brabec T 2015 *Phys. Rev. B* **91** 064302
[25] Ikemachi T, Shinohara Y, Sato T, Yumoto J, Kuwata-Gonokami M and Ishikawa K L 2017 *Phys. Rev. A* **95** 043416
[26] Tancogne-Dejean N, Mücke O D, Kärtner F X and Rubio A 2017 *Phys. Rev. Lett.* **118** 087403
[27] Floss I, Lemell C, Wachter G, Smejkal V, Sato S A, Tong X M, Yabana K and Burgdörfer J 2018 *Phys. Rev. A* **97** 011401
[28] Sato S A, Hirori H, Sanari Y, Kanemitsu Y and Rubio A 2021 *Phys. Rev. B* **103** L041408
[29] Armitage N, Mele E and Vishwanath A 2018 *Rev. Mod. Phys.* **90** 015001
[30] Hu J, Xu S Y, Ni N and Mao Z 2019 *Annual Review of Materials Research* **49** 207
[31] Mics Z, Tielrooij K J, Parvez K, Jensen S A, Ivanov I, Feng X, Müllen K, Bonn M and Turchinovich D 2015 *Nat. Commun.* **6** 7655
[32] Yoshikawa N, Tamaya T and Tanaka K 2017 *Science* **356** 736
[33] Hafez H A, Kovalev S, Deinert J C, *et al.* 2018 *Nature* **561** 507
[34] Shan Y, Li Y, Huang D, Tong Q, Yao W, Liu W T and Wu S 2018 *Sci. Adv.* **4** eaat0074
[35] Tancogne-Dejean N and Rubio A 2018 *Sci. Adv.* **4** eaao5207
[36] Alonso Calafell I, Rozema L A, Alcaraz Iranzo D, *et al.* 2021 *Nat. Nanotechnol.* **16** 318
[37] Cheng B, Kanda N, Ikeda T N, Matsuda T, Xia P, Schumann T, Stemmer S, Itatani J, Armitage N and Matsunaga R 2020 *Phys. Rev. Lett.* **124** 117402
[38] Huang S M, Xu S Y, Belopolski I, *et al.* 2015 *Nat. Commun.* **6** 7373
[39] Weng H, Fang C, Fang Z, Bernevig B A and Dai X 2015 *Phys. Rev. X* **5** 011029
[40] Murakami S, Hirayama M, Okugawa R and Miyake T 2017 *Sci. Adv.* **3** e1602680
[41] Lv B, Weng H, Fu B, *et al.* 2015 *Phys. Rev. X* **5** 031013
[42] Lv B, Xu N, Weng H, Ma J, *et al.* 2015 *Nat. Phys.* **11** 724
[43] Xu S Y, Belopolski I, Sanchez D S, *et al.* 2015 *Sci. Adv.* **1** e1501092

[44] Arnold F, Naumann M, Wu S C, Sun Y, Schmidt M, Borrmann H, Felser C, Yan B and Hassinger E 2016 *Phys. Rev. Lett.* **117** 146401
[45] Xu S Y, Belopolski I, Alidoust N, *et al.* 2015 *Science* **349** 613
[46] Xu N, Weng H, Lv B, *et al.* 2016 *Nat. Commun.* **7** 11006
[47] Xu Y, Zhang F and Zhang C 2015 *Phys. Rev. Lett.* **115** 265304
[48] Soluyanov A A, Gresch D, Wang Z, Wu Q, Troyer M, Dai X and Bernevig B A 2015 *Nature* **527** 495
[49] Sodemann I and Fu L 2015 *Phys. Rev. Lett.* **115** 216806
[50] Ma Q, Xu S Y, Shen H, *et al.* 2019 *Nature* **565** 337
[51] Kang K, Li T, Sohn E, Shan J and Mak K F 2019 *Nat. Mater.* **18** 324
[52] Lai S, Liu H, Zhang Z, *et al.* 2021 *Nat. Nanotechnol.* **16** 869
[53] Wang C, Xiao R C, Liu H, *et al.* 2022 *Natl. Sci. Rev.* **2022** nwac020
[54] Rostami H and Polini M 2018 *Phys. Rev. B* **97** 195151
[55] McIver J W, Schulte B, Stein F U, Matsuyama T, Jotzu G, Meier G and Cavalleri A 2020 *Nat. Phys.* **16** 38
[56] Xu H, Zhou J and Li J 2021 *Adv. Sci.* **8** 2101508
[57] Bharti A, Mrudul M and Dixit G 2022 *Phys. Rev. B* **105** 155140
[58] Chan C K, Lindner N H, Refael G and Lee P A 2017 *Phys. Rev. B* **95** 041104
[59] Sirica N, Tobey R, Zhao L, *et al.* 2019 *Phys. Rev. Lett.* **122** 197401
[60] Sirica N, Orth P P, Scheurer M, *et al.* 2022 *Nat. Mater.* **21** 62
[61] Bhalla P and Rostami H 2022 arXiv:2201.00734 [condmat.mes-hall]
[62] de Juan F, Grushin A G, Morimoto T and Moore J E 2017 *Nat. Commun.* **8** 15995
[63] Wang Q, Zheng J, He Y, *et al.* 2019 *Nat. Commun.* **10** 5736
[64] Ma J, Gu Q, Liu Y, Lai J, Yu P, Zhuo X, Liu Z, Chen J H, Feng J and Sun D 2019 *Nat. Mater.* **18** 476
[65] Lv Y Y, Xu J, Han S, *et al.* 2021 *Nat. Commun.* **12** 6437
[66] Ishikawa K L 2010 *Phys. Rev. B* **82** 201402
[67] Lim J, Ang Y S, de Abajo F J G, Kaminer I, Ang L K and Wong L J 2020 *Phys. Rev. Research* **2** 043252
[68] Ikeda T N 2020 *Phys. Rev. Research* **2** 032015
[69] O'Brien T, Diez M and Beenakker C 2016 *Phys. Rev. Lett.* **116** 236401
[70] Yu Z M, Yao Y and Yang S A 2016 *Phys. Rev. Lett.* **117** 077202
[71] Ishikawa K L 2013 *New J. Phys.* **15** 055021
[72] Chizhova L A, Libisch F and Burgdörfer J 2016 *Phys. Rev. B* **94** 075412
[73] Ikeda T N, Chinzei K and Tsunetsugu H 2018 *Phys. Rev. A* **98** 063426
[74] Carbotte J 2016 *Phys. Rev. B* **94** 165111
[75] Neufeld O, Podolsky D and Cohen O 2019 *Nat. Commun.* **10** 405
[76] McCormick T M, Kimchi I and Trivedi N 2017 *Phys. Rev. B* **95** 075133
[77] Osterhoudt G B, Diebel L K, Gray M J, *et al.* 2019 *Nat. Mater.* **18** 471
[78] Gao Y, Kaushik S, Philip E, *et al.* 2020 *Nat. Commun.* **11** 720